On the thermo-mechanical stability and oxidation behavior of carbon S-phase at elevated temperature and under tensile stress

Li, W.; Li, X.; Chiu, Y.-l.; Dong, H.

DOI:
10.1016/j.msea.2014.02.013

Document Version
Publisher's PDF, also known as Version of record

Citation for published version (Harvard):
Li, W, Li, X, Chiu, Y & Dong, H 2014, 'On the thermo-mechanical stability and oxidation behavior of carbon S-phase at elevated temperature and under tensile stress', *Materials Science and Engineering A*, vol. 600, pp. 90-98. https://doi.org/10.1016/j.msea.2014.02.013

Materials Science & Engineering A 600 (2014) 90–98

Contents lists available at ScienceDirect

Materials Science & Engineering A

journal homepage: www.elsevier.com/locate/msea

On the thermo-mechanical stability and oxidation behavior of carbon S-phase at elevated temperature and under tensile stress

W. Li [a,b,*], X. Li [a], Y.-L. Chiu [a], H. Dong [a]

[a] School of Metallurgy and Materials, The University of Birmingham, Birmingham B15 2TT, UK
[b] School of Materials Science and Engineering, Shanghai Jiaotong University, Shanghai 200240, China

ARTICLE INFO

Article history:
Received 17 October 2013
Received in revised form
10 December 2013
Accepted 4 February 2014
Available online 12 February 2014

Keywords:
Plasma carburizing
S-phase
Stability
Tensile stressing
Oxidation

ABSTRACT

The thermo-mechanical stability and oxidation behavior of S-phase are critical issues for some industrial applications at elevated temperatures owing to its metastable nature. In this study, the stability and oxidation behavior of carbon S-phase generated by plasma carburizing on AISI316 under both thermal and mechanical conditions was investigated for the first time. The experimental results demonstrate that when tested at a fixed temperature the thickness of the carbon S-phase layer increased with the stress applied to the tensile specimens during the thermo-mechanical stability tests. This indicates that tensile stress promotes the diffusion of carbon in the carbon-S-phase. The oxidation resistance of the carbon S-phase at 500 °C is inferior to untreated AISI 316, which further deteriorated under tensile stress. The lattice expansion and high density of crystal defects in the S-phase and the applied tensile stress would facilitate the diffusion of oxygen and iron, thus promoting oxidation.

1. Introduction

Due to their good ductility, adequate strength, good weldability and excellent resistance to corrosion, austenitic stainless steels (ASS) are widely used in many industrial sectors, such as nuclear power stations and biomedical devices. However, the relative low hardness of these materials has impeded their tribological applications which require good wear resistance and high load bearing capacity [1]. Therefore, the enhancement of the surface properties of ASSs has been an important research subject from both a scientific and a technological point-of-view.

It has been reported that thermo-chemical treatments (such as nitriding or carburizing) of ASSs at relative low temperatures (below about 500 °C for carburizing and even lower for nitriding) can form an interstitial (C, N or both C and N) supersaturated (up to about 12 at% C or 25 at% N) but precipitation-free layer [2] with combined improvements in hardness [3], wear resistance, fatigue properties [4] and corrosion resistance [5–9]. This layer was called S phase [10,11] or expanded austenite [12,13].

Notwithstanding the fact that S-phase exhibits excellent combination of mechanical, tribological and corrosion properties and has found some important applications [14], S-phase is thermodynamically and kinetically metastable with supersaturated interstitials such as C and N in austenitic stainless steel [6,15]. In essence, S-phase is thermodynamically metastable and will change to more stable phases under certain favorable conditions [16]. For example, Li et al. [17,18] have reported that precipitation of chromium carbides or nitrides occurred when S-phase was annealed above a certain level of temperatures. Consequently, S-phase was decomposed into more stable phases [19] (such as austenite, ferrite, nitrides or carbides) and its corrosion resistance deteriorated dramatically due to the depletion of chromium necessary for the stainlessness of ASSs [20].

However, the effect of stressing at elevated temperature on the thermo-mechanical stability of S-phase has not yet been investigated. The study on the thermo-mechanical stability of the S-phase has real value in some engineering applications. For example, S-phase surface engineered AISI 316 austenitic stainless steel tubes have been used in nuclear reactors and wind turbines under combined actions of elevated temperature, mechanical loading and corrosive environments [14,21,22]. In addition, to date, no work has been reported on the oxidation behavior of S-phase at elevated temperature or under combined effect of temperature and tensile stress. Therefore, it is necessary to study the thermo-mechanical stability and oxidation behavior of S-phase surface engineered austenitic stainless steels under both stress and temperature to advance scientific understanding of the mechanism involved and to identify windows for their safe use in service, which formed the purpose of this research.

* Corresponding author at: School of Materials Science and Engineering, Shanghai Jiaotong University, Shanghai 200240, China. Tel.: +86 21 54745567; fax: +86 21 54745560.
E-mail address: weilee@sjtu.edu.cn (W. Li).

http://dx.doi.org/10.1016/j.msea.2014.02.013
0921-5093

2. Experimental

The material investigated was hot rolled AISI 316 stainless steel sheet with a thickness of 3 mm, the chemical composition of which is listed in Table 1. The samples were cut to a conventional 'dog-bone' shape by electric discharge machining (Fig. 1). Low-temperature plasma carburizing treatment was carried out in a 40 kW Klöchner DC plasma vacuum unit at 500 °C for 10 h in a gas mixture of 1.5% CH_4 and 98.5% H_2 at 400 Pa (coded as PC hereafter).

To study the thermo-mechanical stability and oxidation behavior of the S-phase, specimens were positioned within grips and heated to test temperatures up to 500 °C (which is the threshold temperature for carbon S-phase to avoid thermal decomposition) in a creep tester under different loads. The maximum tensile stress produced in the specimens was 200 MPa, which is below the critical yielding strength of AISI 316 stainless steel to avoid plastic deformation. Therefore, the thermo-mechanical stability tests were carried at 400 °C for 150 h and at 450 and 500 °C for 100 h under a tensile stress of 0, 100 and 200 MPa. The designed testing parameters and sample codes are listed in Table 2.

Specimens were systematically characterized before and after the thermo-mechanical stability tests using Philips XL30 scanning electron microscope (SEM), Jeol 7000 field Emission Gun SEM with wavelength dispersive X-ray spectrometry(WDS), Philips X'Pert diffractometer and FEI Tecnai F20 Field emission transmission electron microscopy (TEM). Plan-view TEM specimen was prepared to study the microstructure of the tested S-phase. The samples were cut and mechanically thinned from the substrate side to ≈80 μm, punched into a 3 mm diameter disc and then reduced to ≈20 μm by a dimple grinder. Final thinning was accomplished in the depth of 10 μm by ion-beam milling in a precision ion polishing system (PIPS) from both sides until perforation occurred. In order to study the thickness and structure of the surface oxide films formed during the thermo-mechanical stability tests, cross-sectional TEM samples were also prepared. Samples were sectioned into 2 slabs 3 mm wide and 1.5 mm thick. The slabs were then glued using G-1 epoxy with the treated surface facing each other. Then the two glued slabs were slowly and carefully ground from both sides down to 100 μm. After that the two pieces of thin slabs with surface layer remaining intact were separated and put into a Quanta 3D Filed Emission Gun (FEG) focused ion beam (FIB) miller for further preparation. Prior to milling, tungsten coating was along the surface of the region from which the sample was to be thinned in order to promote uniform milling and preserve the surface layer. Milling was performed with low beam currents from 15 nA to 5 nA at 30 kV and final thinning at 1 nA to 0.1 nA at 30 kV, finished with a final polish milling at 5 kV 48 pA.

The surface hardness of the specimens before and after the thermo-mechanical stability tests was measured by a Mitutoyo MVK-H1 micro-hardness machine with a diamond Vicker's indenter under 25 g.

Table 1
Composition of the 316 stainless steel sheet (wt%).

C	Cr	Ni	Mn	Mo	Si	Fe
0.03	17.35	10.34	1.62	1.86	0.69	Balance

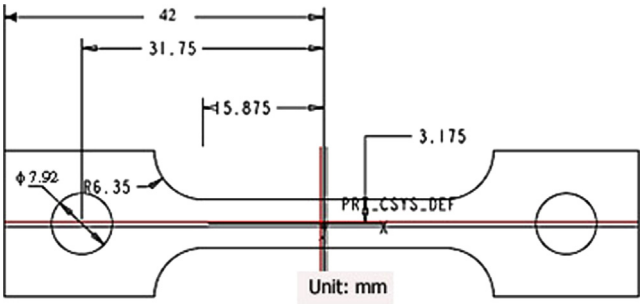

Fig. 1. Schematic drawing of specimen.

Table 2
Conditions for thermo-mechanical stability tests.

Samples code	Temperature (°C)	Tensile stress (Mpa)	Enduring time (h)
UT[a]	–	–	–
UT500 0 Mpa	500	0	100
UT500 200 Mpa	500	200	100
PC[b]	–	–	–
PC400 0 Mpa	400	0	150
PC400 100 Mpa	400	100	150
PC400 200 Mpa	400	200	150
PC450 0 Mpa	450	0	100
PC450 100 Mpa	450	100	100
PC450 200 Mpa	450	200	100
PC500 0 Mpa	500	0	100
PC500 100 Mpa	500	100	100
PC500 200 Mpa	500	200	100

[a] Untreated 316.
[b] As-plasma carburized.

3. Results

3.1. Evolution of surface layer structure

Fig. 2a shows the cross-sectional SEM micrograph of the as-carburized PC 10 samples and it can be seen that a featureless homogenous surface S-phase layer was formed during plasma carburizing at 500 °C for 10 h. No appreciable change in the layer microstructure was observed when the PC 10 h sample was annealed at 400 °C for 150 h under tensile stresses ranging from 0 to 200 MPa.

However, comparing Fig. 2a for PC with Fig. 2b (PC450 0 MPa) and e (PC500 0 MPa) revealed that the thickness of the surface S-phase layer of the as-carburized PC sample increased following 100 h annealing at 450 and 500 °C even without tensile stress. In general, it is apparent that the surface layer was expanded with the increment of temperature.

When annealed under tensile stress, a very thin superficial layer was observed for both 450 °C/100 h (Fig. 2c and d) and 500 °C/100 h (Fig. 2f & g) annealed samples, the thickness of which was increased with increasing the tensile stress from 0 to 200 MPa. In addition, the contrast between the main surface S-phase layer and the substrate became larger when annealed under tensile stress. The grain boundaries and slipping bands can be easily seen in all the thermo-mechanically tested samples under combined temperature and stress. The higher the tensile stress was applied, the clearer these features became when annealed at the same temperature.

3.2. Change of the phase and lattice parameter in surface layers

XRD analysis was conducted on all the samples and Fig. 3a shows the XRD charts of untreated substrate (UT), as-carburized sample (PC) and 500 °C/100 h annealed samples without stress (PC500 0 MPa) and with 100 MPa (PC500 100 MPa) and 200MPA (PC500 200 MPa) tensile stress.

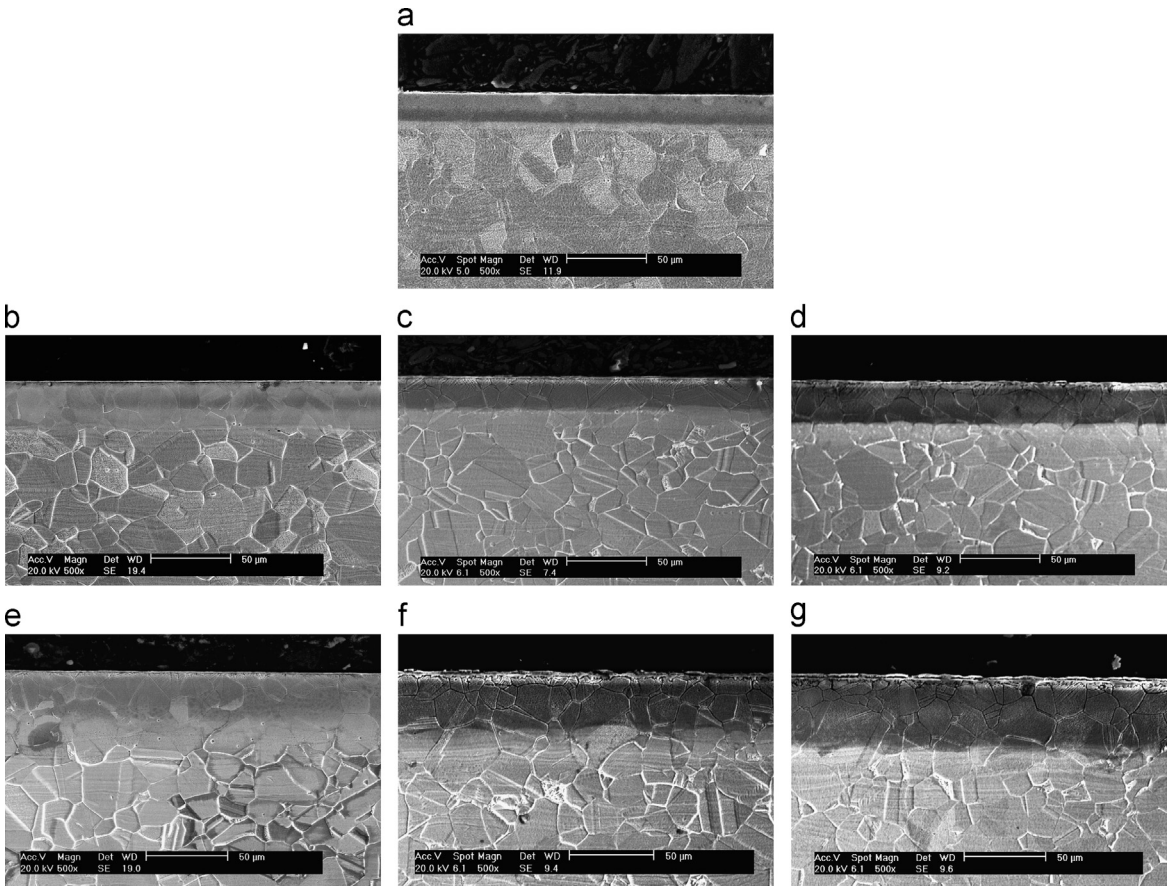

Fig. 2. SEM cross-sectional morphologies of (a) as-carburized PC; PC after 450 °C/100 h annealing under (b) 0 MPa (PC450 0 MPa), (c) 100 MPa (PC450 100 MPa) and (d) 200 MPa (PC450 200 MPa); and PC after 500 °C/100 h annealing under (e) 0 MPa (PC500 0 MPa), (f) 100 MPa (PC500 100 MPa) and (g) 200 MPa (PC500 200 MPa).

As observed by other researchers [23], the carburized PC samples illustrated left-shift of peak positions comparing with the typical 316 stainless steel indicating the formation of a carbon supersaturated expanded austenite (i.e. S-phase) layer. No peaks for any precipitates were detected by the X-ray diffratograms. Minor peaks of iron oxides Fe_2O_3 and Fe_3O_4 were identified from the XRD charts for the 450 and 500 °C annealed samples especially when they were stressed. This is in line with the existence of the very thin superficial layer shown in Fig. 2. These oxides were formed due to oxidation of the sample surfaces during the annealing in air. In general, the intensity of these oxide peaks increased with increasing the tensile stress level. Clearly, the applied tensile stresses promoted the formation of such oxide layers.

The lattice parameter of the expanded austenite in the S-phase layers was obtained by the plot of $a_{(hkl)}$ against $\cos\theta_{(hkl)}{}^{*}\cot\theta_{(hkl)}$, where $a_{(hkl)}$ is the lattice parameter value estimated from the peak indexed by (hkl) and $\theta_{(hkl)}$ is the Bragg angle. Fig. 3b shows a Nelson–Riey plot obtained from the XRD charts. All the experimental data for the annealed samples fall between that for the untreated UT 316 and that for carburized samples (fitted by lines). There existed a tendency that with increasing temperature and stress, the lattice parameter $a_{(hkl)}$ moved towards the value for the untreated state.

3.3. Carbon and hardness distribution

To study the carbon distribution in these annealed samples with or without tensile stress, WDX analysis was carried out to detect the carbon concentrations along the depth of the carburized S-phase layer before and after the thermo-mechanical stability tests. Some representative results were given in Fig. 4. From these profiles, the carbon concentration at the top surface of the as plasma carburized 316ASS was detected to be 3.8 wt%, which decreased rapidly to 0.8 wt% at 5 μm in depth and then gradually approached the substrate value at a depth about 35 μm. Carbon was dissipated to about 1.13 and 0.75 wt% after 100 h thermal annealing at 450 and 500 °C, respectively. The carbon profiles agreed well with the SEM images in terms of the thickness of the carburized layer. For example, the thickness of the carburized layer after thermal annealing at 500 °C for 100 h was estimated to be about 50 μm from Fig. 2e, which is in line with the value obtained from the carbon profile for 500 °C/100 h thermal annealed PC500 0 MP sample showed in Fig. 4. The effect of tensile stress on annealing could be deducted by comparing the carbon depth distribution after annealing at 450 °C for 100 h with and without tensile stressing. It can be seen from Fig. 4 that although the surface carbon content was reduced after 450 °C/100 h annealing under 0 (unstressed) and 200 MPa (stressed) tensile stress, the surface carbon content was 1.13 and 0.92 wt% respectively for unstressed PC450 0 MPa and stressed PC450 200 MPa samples. The difference in the surface carbon content of these two samples seems not significant when taking account of the potential apparatus error of $\pm 0.2\%$ for carbon. However, as shown in Fig. 5a, the surface hardness of PC450 0 MPa is still higher than that for PC450 200 MPa, which is in line with the average surface carbon content of these two samples. Therefore, the applied tensile stress could accelerate the diffusion of carbon atoms during thermo-mechanical annealing.

The effect of the thermo-mechanical stability tests on the hardness distribution is depicted in Fig. 5. In general, the hardness of the plasma carburized PC sample reduced after the thermo-mechanical

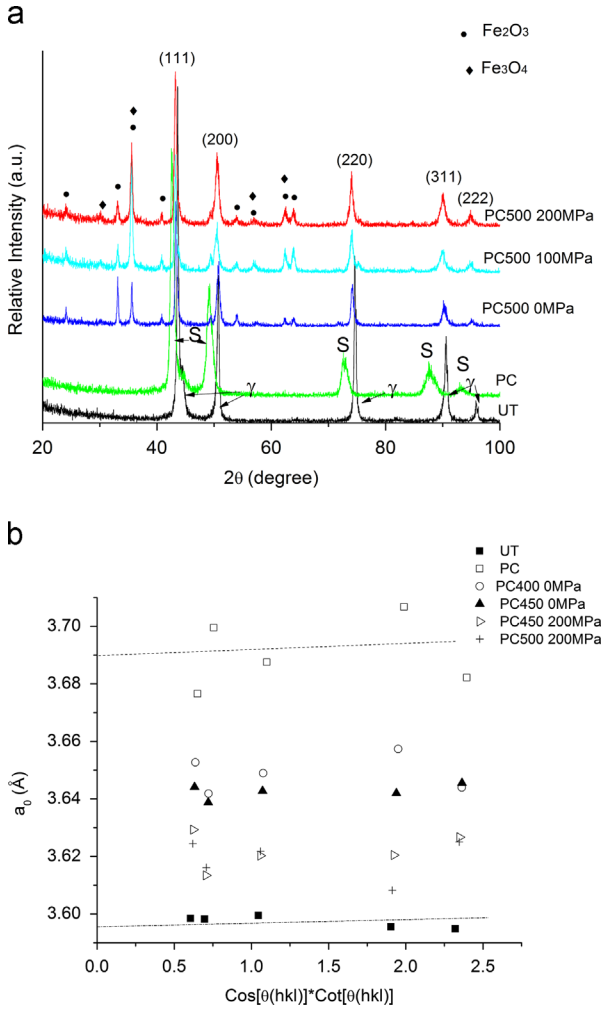

Fig. 3. (a) XRD patterns of PC treated 316ASS and after annealing for 100 h at 500 °C under 0, 100 and 200 MPa tensile stresses. (b) Nelson–Riley plots and fitting curves for measuring the lattice expansion of untreated 316 substrate (UT), as-carburized S-phase (PC) and annealed samples with or without tensile stressing.

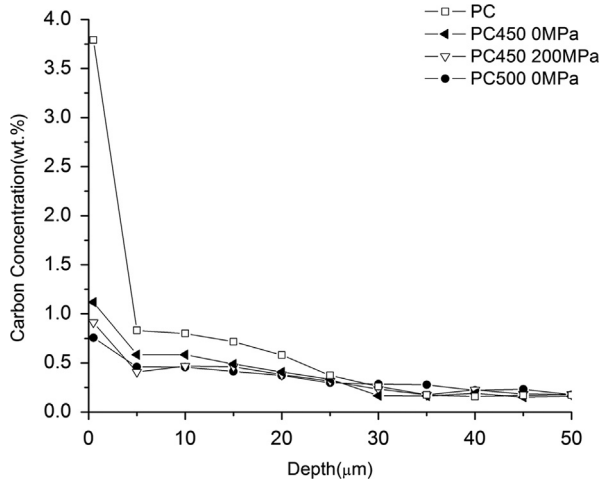

Fig. 4. Carbon profiles along the cross sectional samples of as plasma carburized PC and after annealing under different tensile stresses for 100 h.

tests. This is mainly because without the constant supply of carbon, the supersaturated carbon in the S-phase underwent diffusion both outward and inward, thus reducing its hardness. Meanwhile, the oxidation observed at the surface layers of the samples annealed

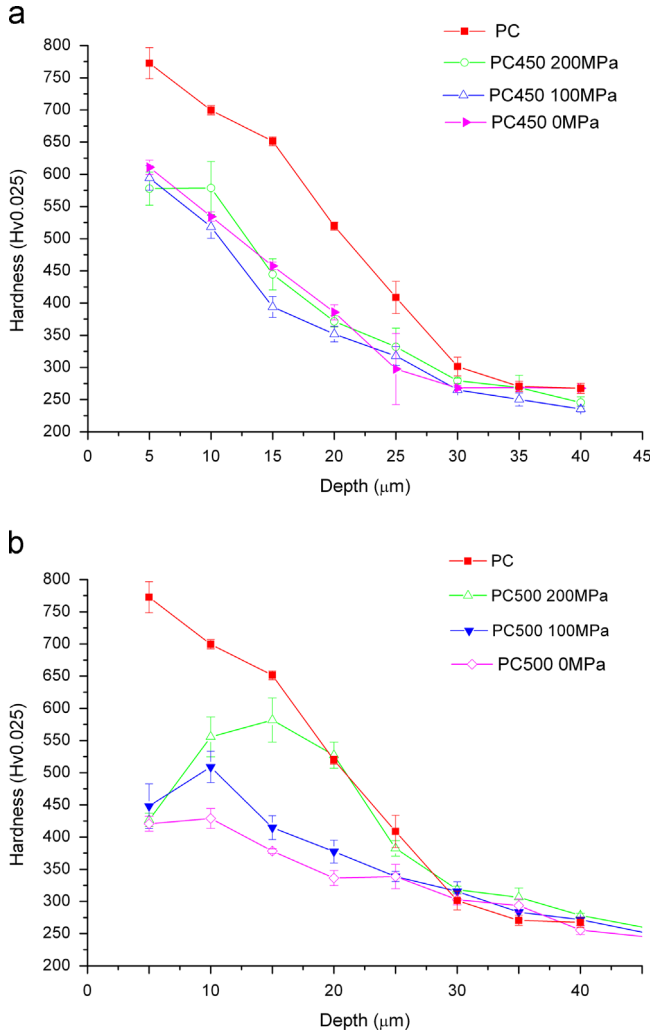

Fig. 5. Effect of tensile stress on the hardness profiles along the cross sectional samples after (a) 450 °C/100 h and (b) 500 °C/100 h annealing.

under tensile stresses may also have contributed to the decrease in surface carbon content. However, two interesting features were noticed from Fig. 5. Firstly, whilst the low- and medium-temperature annealed samples, whether stressed or not, showed a gradual reduction of the hardness with the depth (Fig. 5a), the high-temperature (500 °C) annealed samples displayed a sigmoid distribution (Fig. 5b). Secondly, the application of a tensile stress during annealing of S-phase layer can retard the deduction of its hardness in particular for the 500 °C annealed samples. For example, the hardness at the depth of 20 μm was about $320HV_{0.025}$ for PC500 0 MPa (without applied stress) while that of PC500 200 MPa (with 200 MPa tensile stress) was about $520HV_{0.025}$, which is the same as that for the as-carburized PC sample at the same depth.

To understand the hardening mechanism of the sample annealed at 500 °C for 100 h under a tensile stress of 200 MPa in the depth of 10–20 μm, plan-view TEM was conducted. High density dislocations, micro twins and array of nano-twins were observed in the surface layer, which are normally observed in the deformed microstructure of metals with low stacking fault energy (SFE < 20 mJ/m^2 for 316 stainless steel). Fig. 6a presents the TEM bright-field images of micro twins at both sides of a grain boundary and entangled dislocations within the grains. Corresponding selected area diffraction pattern indicated S-phase matrix with micro twins of [1$\bar{1}$0] zone patterns. Fig. 6b shows nanotwins within the annealed and stressed surface layer. These

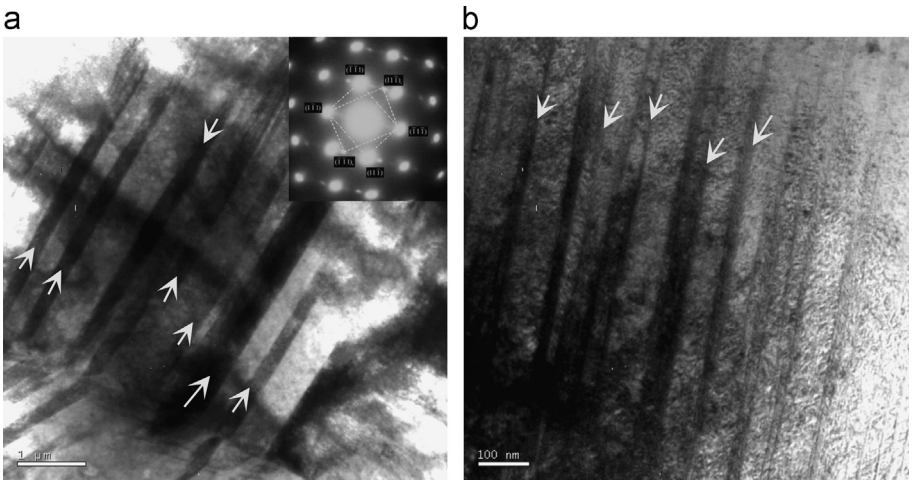

Fig. 6. Plan view TEM bright field microscopy of sample '500 200 MPa' (a) micro $\langle 1\bar{1}0\rangle$twining and (b) nano twining (denoted by errors).

high density defects could have contributed to the strengthening effect observed in Fig. 5b.

3.4. Oxidation behavior

The oxidation behavior of carbon S-phase was compared with as-received 316 materials by annealing the UT and PC samples in air at 500 °C for 100 h with or without tensile stress.

SEM observation and EDX line scan were conducted on the cross-sections of the oxidized samples. Fig. 7 shows the SEM cross-sectional layer structure of 500 °C/100 h annealed as-received 316 under 200 MPa tensile stress (i.e. UT500 200 MPa, Fig. 7a), 500 °C/100 h annealed PC sample without stress (i.e. PC500 0 MPa, Fig. 7b) and the 500 °C/100 h annealed PC sample under 200 MPa tensile stress (i.e. PC500 200 MPa, Fig. 7c). The surface oxide layer formed on the as-received 316 sample after 500 °C/100 h without stressing is too thin to be revealed by SEM and its TEM cross-sectional layer structure is shown in Fig. 8. The oxide layer under TEM has a bright contrast beneath the black protective layer of tungsten and the thickness of this oxide layer is about 15 nm.

The following observations could be made from Figs. 7 and 8. Firstly, when annealed at 500 °C for 100 h in air the oxide film formed on untreated UT500 0 MPa is only about 15 nm while the oxide layer formed on carbon S-phase is about 1000 nm, which is about 67 times that formed on untreated 316. Clearly, the carbon-S-phase possesses a much lower resistance to oxidation at 500 °C for 100 h than the as-received 316 material. Secondly, when applying 200 MPa tensile stress during 500 °C/100 h annealing in air, the thickness of the surface oxide film formed on the untreated 316 and the carbon S-phase increased to about 50 nm and 1800 nm, respectively. Obviously, the applied tensile stress promoted the formation of oxide layer on both the untreated 316 and the carbon S-phase.

As shown in Fig. 3a, two types of iron oxides, Fe_2O_3 and Fe_3O_4, were identified by XRD from the surface of 500 °C/100 h annealed S-phase samples; in contrast, only Cr_2O_3 was detectable by TEM (Fig. 8) and XRD (Fig. 9) from the surface of 500 °C/100 h annealed 316 without and with tensile stress, respectively.

In order to gain further insights into the oxidation of S-phase, further EDX and TEM investigation were conducted. Fig. 10 shows typical SEM EDX line scan results for 500 °C/100 h annealed S-Phase sample (PC500 0 MPa) and it can be seen that in general the surface layer is rich in chromium and oxygen and lean in iron and nickel. Close examination also revealed that the inner part of the oxide contained slightly higher chromium than the outer part of the oxide layer.

Representative cross sectional TEM microstructure of the oxide layer formed on the PC500 200 MPa sample is shown in Fig. 11. It can be see that the single oxide layer shown in SEM micrograph (Fig. 7b and c) contained two oxide sublayers with different contrast under TEM. The SAD analysis revealed that the outer layer contains mainly Fe_3O_4 -like oxide with a grain size of 20–50 nm, whilst the inner layer is mainly contains Fe_2O_3-like oxide. However, some Fe_2O_3-like oxide was embedded in the Fe_3O_4-like layer (Fig. 12). The composition of these oxide layers was detected by EDX with a fine beam of about 3 nm and the results are listed in Table 3. Clearly, these oxides contained a certain amount of chromium and the outer oxide and the inner oxide could be denoted as $(Fe_4Cr)_3O_4$ and $(Fe_2Cr)_2O_3$ oxide, respectively with the former (the outer oxide layer) containing less Cr than the latter (the inner oxide layer). This is in line with the EDX line scan results shown in Fig. 10.

4. Discussion

In some industrial applications, uniaxial tensile stress is a very common stress status for structural components. For example, as reported by Lebrun et al. S-phase surface engineered thin (10 mm in diameter) and long (3.8–4.4 m in length) 316 austenitic stainless steel tubes have been used in control rod cluster in pressurized water nuclear reactor under joint tensile stressing at elevated temperatures [21]. S-phase surface engineered corrosion resistant alloys including austenitic stainless steel, Co–Cr alloys and Ni–Cr alloys also have great potential for the oil and gas and other industries where both tensile stress and elevated temperature are involved. Therefore the stability and the oxidation behavior of S-phase during long exposures to heat and tensile stress are essential for scientific advancement and technology development.

4.1. Effect of tensile stressing on carbon diffusion and hardness

As shown in Fig. 3b, there exists a tendency that with increasing temperature and tensile stress, the lattice parameter $a_{(hkl)}$ becomes smaller and gradually approaches the untreated state. This is mainly because the carbon content in the S-phase was decreased by increasing the temperature and tensile stress as evidenced in Fig. 4. The effect of applied tensile stress on the

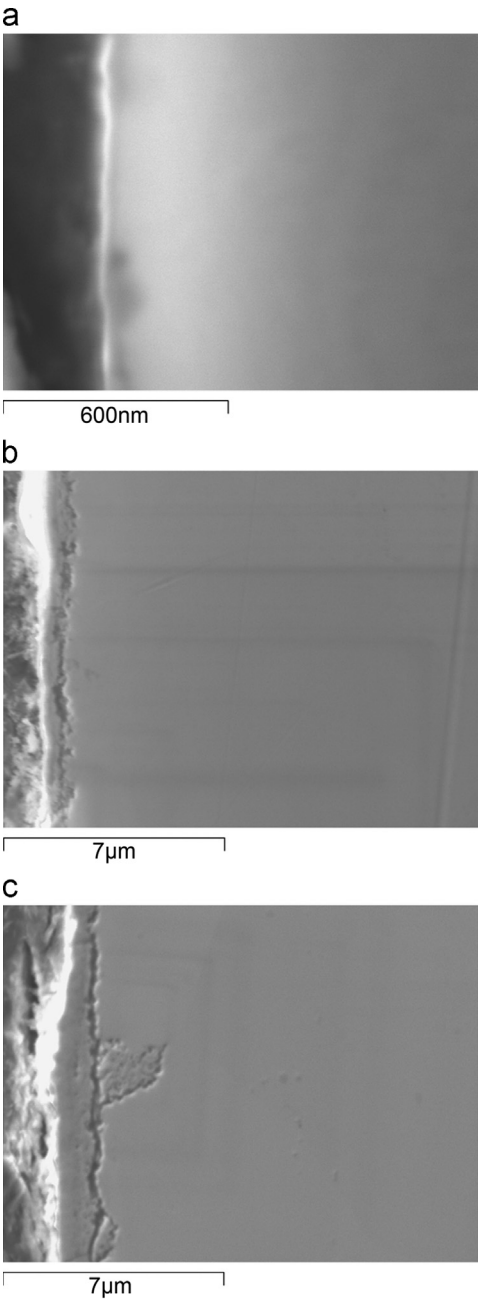

Fig. 7. XSEM micrographs showing oxide layer formed on 500 °C/100 h annealed (a) UT500 200 MPa, (b) PC500 0 MPa and (c) PC500 200 MPa samples.

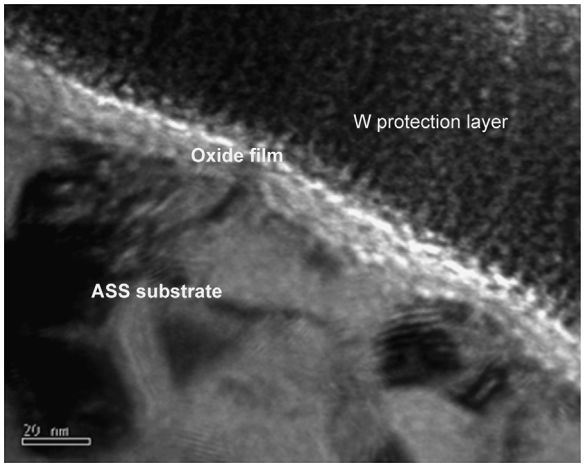

Fig. 8. Cross sectional TEM images from UT500 0 MPa sample.

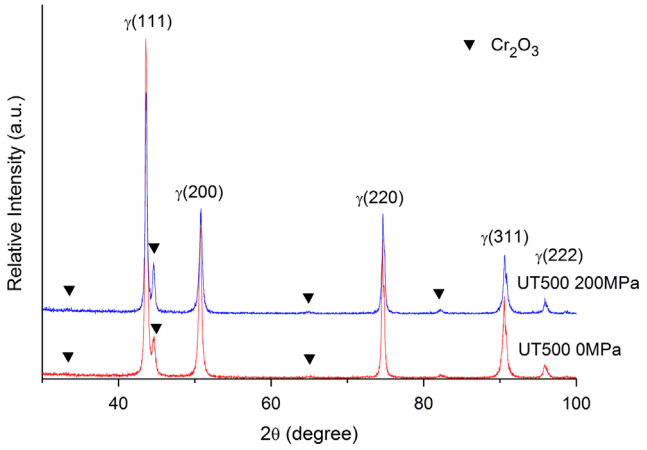

Fig. 9. XRD chart of 500 °C/100 h annealed 316 with 200 MPa tensile stress (UT500 200 MPa).

lattice parameter a_0 can be demonstrated by the Nelson–Riley plots for 450 °C/100 h annealed samples without stress and with 200 MPa tensile stress (PC450 200 Mpa). This implies that the tensile stress does accelerate the carbon diffusion overall in the S-phase during the annealing process.

As reported in our previous paper [24], the diffusion activation energy of carbon in 316 reduced from 142.76 to 133.91 $KJmol^{-1}$ when a tensile stress of 40 Mpa was in-situ applied during plasma carburizing at temperatures ranging from 400 to 450 °C. Therefore, the tensile stresses applied to the sample during plasma carburizing made the diffusion of carbon easier and hence faster. This is mainly because the very high level compressive residual stress caused by supersaturation of carbon in the carbon S-phase [7,25] could be partially canceled by the applied tensile stress [24]. In this study, a higher level of tensile stress of 100–200 MPa was applied during the annealing of carbon S-phase in air and hence more significant effect could be expected.

It has been generally accepted that the S-phase hardening could attributed to solid solution hardening and defect-related hardening [12]. Of course precipitation could also influence the hardness of S-phase layer, but it is excluded in this case because no precipitates were found by any characterization methods in these samples.

For solid solution hardening, it is known that the higher the carbon absorbed, the higher hardness it exhibits. The solid solution strengthening is considered as one of the most important hardening mechanisms because of the high level of interstitial elements (such as carbon) in the S-phase. This explained the high hardness of S-phase comparing to the untreated austenite [26]. When annealed at a high temperature, the carbon concentration decreased (Fig. 4) and hence the solid solution strengthening effect is diminished and the hardness would drop.

Similar to work-hardening mechanism, the second possible strengthening mechanism could be based on interaction between crystal defects. It is of interest to note that although the carbon depth profile of PC450 200 MPa is below that of PC450 0 MPa (Fig. 4), their hardness depth distribution is very similar (Fig. 5a). Indeed, the 500 °C annealed samples showed the 'sigmoid' trend in hardness (see Fig. 5b '500 200 MPa'): the hardness increases and then decreases after reaches a peak). This could be explained by the nano-twin-hardening mechanism. This is because, as revealed by TEM results in Fig. 6b, the 'PC500 200 MPa' sample

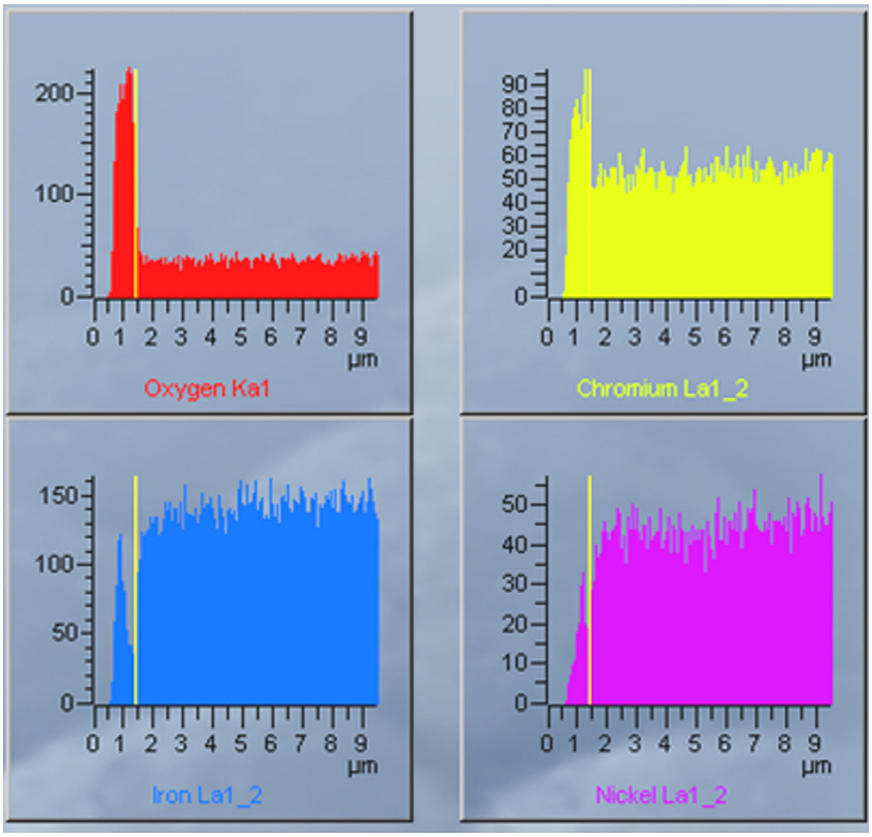

Fig. 10. Cross sectional SEM EDX line scan of PC500 0 MPa sample (the vertical line indicates the interface between the surface oxide film and the S-phase subsurface).

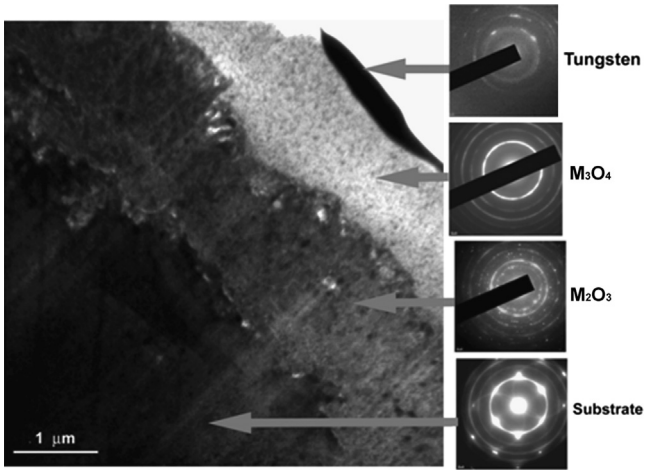

Fig. 11. Cross sectional TEM of oxides layer formed at 500 °C under 200 MPa on PC500 200 MPa sample.

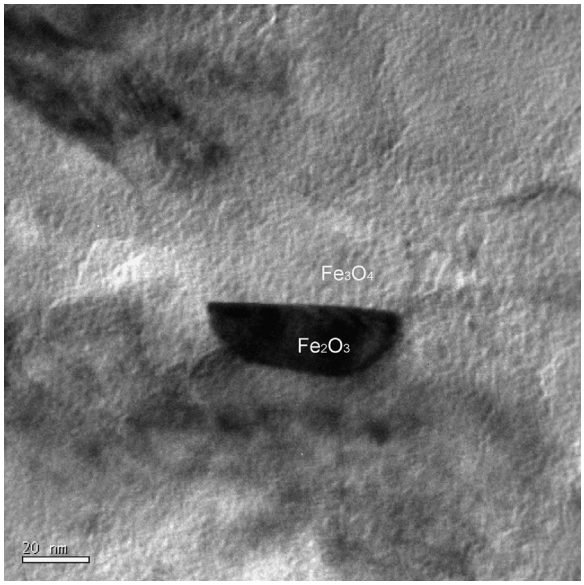

Fig. 12. Nano sized Fe_2O_3 grown into the Fe_3O_4 layer.

contained a high density of nanotwins, and it has been reported that nanotwins can produce very significant hardening in some materials [27].

4.2. Oxidation of S-phase

As reported above, the oxidation behavior of carbon S-phase formed during low-temperature plasma carburizing differs greatly from the untreated AISI316 austenitic stainless steel.

A very thin Cr_2O_3 oxide film about 15 nm was formed on the surface of untreated 316 during 500 °C/100 h annealing in air without stressing (Fig. 8). This is because the outward diffusion of chromium ($Cr3+$) has shown to be faster than the inward

Table 3
EDX Composition (at%) and Cr/Fe ratio of oxide layers and 316 substrate.

Element	Fe_3O_4	Fe_2O_3	316 substrate
O	50.6	50.0	5.0
Cr	7.6	15.6	19.9
Mn	0.7	1.2	1.5
Fe	33.9	26.2	60.3
Ni	2.2	1.7	7.8
Cr/Fe	0.22	0.61	0.33

diffusion of oxygen by a factor of three and so the chromia film usually forms on the surface of untreated 316 sample [28]. The formation of a dense, adherent and slow growing surface Cr_2O_3 oxide film can serve as a diffusion barrier to block the outward diffusion of iron and inward diffusion of oxygen [29]. Therefore, as evidenced in Fig. 9, only Cr_2O_3 oxide was detectable by XRD even after oxidation at 500 °C for 100 h in air. Although the application of a 200 MPa tensile stress during 500 °C/100 h annealing in air increased the thickness of the surface oxide film from 15 to 50 nm, the oxide layer is still very thin (Fig.7a) and predominated by Cr_2O_3 oxide (Fig. 9). This implies that although the applied tensile stress could, to some extent, increase the diffusion of oxygen and chromium most probably due to the lattice expansion under tensile stress, the thin Cr_2O_3 oxide film can still protect the surface from further oxidation.

In contrast, however, the oxide layer formed on the carbon S-phase is much thicker (1000–1800 nm) than that formed on untreated 316 (15–50 nm) when annealed under the same conditions. In addition, Cr-containing iron oxides formed on the annealed carbon S-phase (Fig. 3) while only chromium oxide formed on annealed UT sample (Figs. 8 and 9). Clearly, the oxidation behavior of the carbon S-phase differs greatly from that of the as-received 316 material. This could be attributed to the crystal structure and defects of the carbon S-phase. As indicated in [30], the supersaturated interstitials (such as carbon in carbon S-phase in this study) can cause very large lattice expansion and distortions; what is more, S-phase contains a large amount of crystalline defects such as dislocations and twins (Fig. 6). The large lattice expansion and high density of crystal defects could greatly facilitate the diffusion of oxygen, iron and chromium thus promoting the formation of iron/chromium oxides. It is known that iron oxides provide weak resistance to cation diffusion and Fe ions are more mobile than the Cr ions [31]. Therefore, rapid growth of iron oxides is expected, which makes it difficult to form a dense and continue chromium oxide film. This is evidenced by the formation of Cr-containing iron oxide dual layers (Fig. 11 and Table 3) during the oxidation of the carbon S-phase layer. This is also supported by the fact that the inner oxide layer contains more Cr than the outer oxide layer. In the meantime, substitutional diffusion of Fe and Cr may generate vacancies behind the diffusion direction, which, in turn, could further facilitate the diffusion of oxygen.

It is clear by comparing Fig. 7b with c that the oxidation of carbon S-phase at 500 °C for 100 h was further promoted by applying 200 Mpa tensile stress during the thermo-mechanical stability tests. The applied tensile stress could cause the formation of micro-cracks within the surface oxide layer (Fig. 2c, d, f and g). This is further supported by TEM examination of the surface oxide layer. As shown in Fig. 13a for the zero stressed sample, the Fe_2O_3 particle are uniformly embedded in the Fe_3O_4 matrix and both Fe_2O_3 and Fe_3O_4 particles have a similar size about 40 nm, which could ease any stress concentration; on the other hand, the embedded Fe_2O_3 particles about 24 nm are much smaller than the Fe_3O_4 matrix grains and micro-cracks were observed in the 200 MPa tensile stressed sample (Fig. 13b). The reason for the embedment of Fe_2O_3 particles in Fe_3O_4 is not very clear; however, it is most probably that the applied high tensile stress and the micro-cracks promoted the diffusion of oxygen and hence the transformation of Fe_3O_4 to Fe_2O_3 in some areas.

5. Conclusions

The thermo-mechanical stability and oxidation behavior of S-phase are critical issues for some industrial applications at elevated temperatures owing to its metastable nature. In this study, the stability and oxidation behavior of carbon S-phase generated by plasma carburizing at 500 °C for 10 h on AISI316 under both thermal and mechanical conditions has been investigated for the first time and the following conclusions can be drawn:

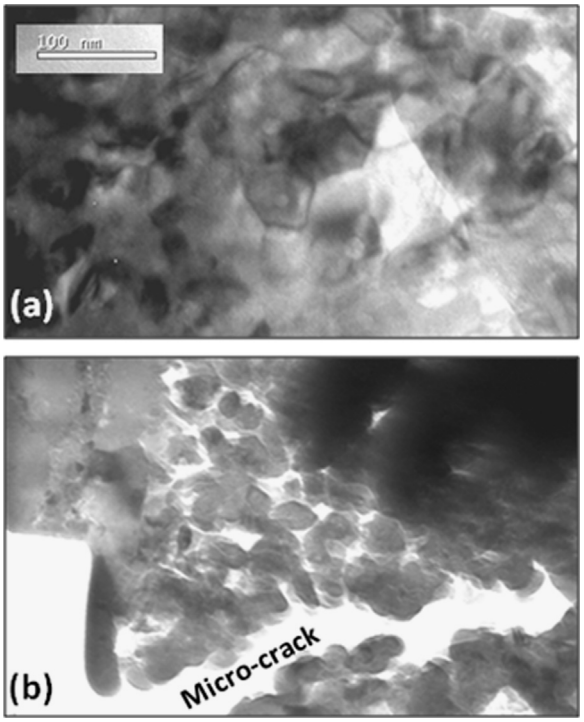

Fig. 13. Oxides layer formed during 500 °C/100 h annealing: (a) without tensile stress and (b)with 200 MPa tensile stress.

- An S-phase surface layer was formed on AISI316 austenitic stainless steel after the plasma carburizing, which significantly increased the hardness of the material.
- No precipitation of chromium carbides can be detectable in the carbon S-phase layer on AISI 316 after thermo-mechanical stability tests up to 500 °C under 200 Mpa tensile stress for 100 h.
- The thickness of the carbon S-phase layers increases with the increase of the temperature and applied tensile stress during thermo-mechanical stability but the opposite occurs to the carbon contents and thus the hardness of the carbon S-phase layer.
- The applied tensile stress can promote the diffusion of carbon during thermo-mechanical stability, which could cancel the level of high residual compressive stress in the carbon S-phase layer.
- Oxidation layers grow much faster during thermo-mechanical stability tests at 500 °C on the carbon S-phase layer than on the untreated 316, which is most likely due to the large lattice expansion and high density of defects in the carbon S-phase.
- While a single Cr_2O_3 oxide thin film formed on untreated 316, chromium-containing iron oxides dual layers formed on the carbon S-phase layer during the thermo-mechanical stability tests.
- The applied tensile stress can promote the growth of surface oxide layer on both the carbon S-phase layer and untreated 316 during the thermo-mechanical stability tests.

Acknowledgments

The authors would like to thank EPSRC, UK (EP/J018252/1) and NSFC, China (51201105) for the financial support. In addition, the

authors wish to express their appreciation to their colleagues, Drs. Jian Chen and Marry Taylor for their technical discussion and support.

References

[1] K.H. Lo, C.H. Shek, J.K.L. Lai, Mater. Sci. Eng. R 65 (2009) 39–104.
[2] J. Oddershede, T.L. Christiansen, K. Ståhl, M.A.J. Somers, Scr. Mater. 62 (2010) 290–293.
[3] J.C. Stinville, P. Villechaise, C. Templier, J.P. Rivière, M. Drouet, Acta Mater. 58 (2010) 2814–2821.
[4] O. Celik, M. Baydogan, E. Atar, E.S. Kayali, H. Cimenoglu, Mater. Sci. Eng. A 565 (2013) 38–43.
[5] J.P. Lebrun, European Patent EP 1000181, 2002.
[6] Y. Cao, F. Ernst, G.M. Michal, Acta Mater. 51 (2003) 4171–4181.
[7] A.H. Heuer, H. Kahn, F. Ernst, G.M. Michal, D.B. Hovis, R.J. Rayne, F.J. Martin, P. M. Natishan, Acta Mater. 60 (2012) 716–725.
[8] Y. Sun, Corros. Sci. 52 (2010) 2661–2670.
[9] J. Buhagiar, A. Spiteri, M. Sacco, E. Sinagra, H. Dong, Corros. Sci. 59 (2012) 169–178.
[10] Z.L. Zhang, T. Bell, Surf. Eng. 1 (1985) 131–136.
[11] K. Ichii, K. Fujimura, T. Takase, Technol. Rep. Kansai Univ. 27 (1986) 135–144.
[12] T. Christiansen, M.A.J. Somers, Scr. Mater. 50 (2004) 35–37.
[13] G.M. Michal, F. Ernst, H. Kahn, Y. Cao, F. Oba, N. Agarwal, A.H. Heuer, Acta Mater. 54 (2006) 1597–1606.
[14] H. Dong, Int. Mater. Rev. 55 (2010) 65–98.
[15] A. Martinavičius, G. Abrasonis, A.C. Scheinost, R. Danoix, F. Danoix, J. C. Stinville, G. Talut, C. Templier, O. Liedke, S. Gemming, W. Möller, Acta Mater. 60 (2012) 4065–4076.
[16] F. Ernst, D. Li, H. Kahn, G.M. Michal, A.H. Heuer, Acta Mater. 59 (2011) 2268–2276.
[17] X.Y. Li, S. Thaiwatthana, H. Dong, Surf. Eng. 18 (2002) 448–452.
[18] X.Y. Li, Y. Sun, T. Bell, Z. Metallkd. 90 (1999) 901–907.
[19] F. Ernst, Y. Cao, G.M. Michal, A.H. Heuer, Acta Mater. 55 (2007) 1895–1906.
[20] T. Christiansen, M.A.J. Somers, Z. Metallkd. 97 (2006) 79–88.
[21] J.P. Lebrun, L. Poirier, D. Hertz, C. Lincot, Surf. Eng. 18 (2002) 423–428.
[22] M. Zlatanovic, N. Popovic, M. Mitric, Thin Solid Films 516 (2007) 228–232.
[23] S. Thaiwatthana, X.Y. Li, H. Dong, T. Bell, Surf. Eng. 18 (2002) 433–437.
[24] W. Li, X.Y. Li, H. Dong, Acta Mater. 59 (2011) 5765–5774.
[25] T. Christiansen, M.A.J. Somers, Mater. Sci. Eng. A 424 (2006) 181–189.
[26] S. Mändl, B. Rauschenbach, J. Appl. Phys. 88 (2000) 3323–3329.
[27] J.R. Greer, Nat. Mater. 12 (2013) 689–690.
[28] R.J. Hussey, D.F. Mitchell, M.J. Graham, Mater. Corros. 38 (1987) 575–585.
[29] D. Young, High Temperature Oxidation and Corrosion of Metals, Elsevier Ltd, Oxford, 2008.
[30] C. Tromas, J.C. Stinville, C. Templier, P. Villechaise, Acta Mater. 60 (2012) 1965–1973.
[31] A.J. Sedriks, Corrosion of Stainless Steel, John Wiley and Sons Inc, Canada, 1966.